Monthly Notices of the ROYAL ASTRONOMICAL SOCIETY
MNRAS **448,** 781–791 (2015) doi:10.1093/mnras/stv054

NGC 2276: a remarkable galaxy with a large number of ultraluminous X-ray sources

Anna Wolter,[1★] Paolo Esposito,[2,3] Michela Mapelli,[4] Fabio Pizzolato[5] and Emanuele Ripamonti[6]

[1] *Osservatorio Astronomico di Brera, INAF, via Brera 28, I-20121 Milano, Italy*
[2] *IASF–Milano, INAF, via E. Bassini 15, I-20133 Milano, Italy*
[3] *Harvard–Smithsonian Center for Astrophysics, 60 Garden Street, Cambridge, MA 02138, USA*
[4] *Osservatorio Astronomico di Padova, INAF, vicolo dell'Osservatorio 5, I-35122 Padova, Italy*
[5] *Dipartimento di Fisica, Università degli Studi di Milano, via G. Celoria 16, I-20133 Milano, Italy*
[6] *Dipartimento di Fisica e Astronomia 'Galileo Galilei', Università degli Studi di Padova, vicolo dell'Osservatorio 3, I-35122 Padova, Italy*

Accepted 2015 January 7. Received 2015 January 7; in original form 2014 September 6

ABSTRACT

The starbusting, nearby ($D = 32.9$ Mpc) spiral (Sc) galaxy NGC 2276 belongs to the sparse group dominated by the elliptical galaxy NGC 2300. NGC 2276 is a remarkable galaxy, as it displays a disturbed morphology at many wavelengths. This is possibly due to gravitational interaction with the central elliptical galaxy of the group. Previous *ROSAT* and *XMM–Newton* observations resulted in the detection of extended hot gas emission and of a single very bright ($\sim 10^{41}$ erg s^{-1}) ultraluminous X-ray source (ULX) candidate. Here, we report on a study of the X-ray sources of NGC 2276 based on *Chandra* data taken in 2004. *Chandra* was able to resolve 16 sources, 8 of which are ULXs, and to reveal that the previous ULX candidate is actually composed of a few distinct objects. We construct the luminosity function of NGC 2276, which can be interpreted as dominated by high-mass X-ray binaries, and estimate the star formation rate (SFR) to be $\sim$5–15 M$_\odot$ yr^{-1}, consistent with the values derived from optical and infrared observations. By means of numerical simulations, we show that both ram pressure and viscous transfer effects are necessary to produce the distorted morphology and the high SFR observed in NGC 2276, while tidal interaction have a marginal effect.

Key words: methods: numerical – galaxies: individual: NGC 2276 – galaxies: star formation – X-rays: binaries – X-rays: galaxies.

1 INTRODUCTION

NGC 2276 is an Sc galaxy belonging to the poor group of galaxies NGC 2300, which is composed of four or five galaxies[1] and dominated by the namesake elliptical galaxy. Here and throughout the paper, we assume a distance[2] to NGC 2276 of 32.9 Mpc and rescale published values to this distance when necessary. The NGC 2300 group is the first in which an X-ray emitting intragroup medium (IGM) was observed (Mulchaey et al. 1993). Observations with *ROSAT* in fact revealed an extended ($\simeq$0.2 Mpc), unusually dense ($\simeq 5.3 \times 10^{-4}$ cm^{-3}), hot ($\simeq$0.9 keV) and relatively metal poor ($\simeq$0.06 Z$_\odot$) intragroup gas halo (Mulchaey et al. 1993; Davis et al. 1996). NGC 2276 is undergoing starburst activity. A number of H II regions were identified in the galaxy, spread throughout its volume (Hodge & Kennicutt 1983; Davis et al. 1997), and many supernovae have been observed in the last 50 yr (e.g. Iskudaryan & Shakhbazyan 1967; Barbon, Cappellaro & Turatto 1989; Treffers et al. 1993; Dimai, Migliardi & Manzini 2005). The star formation rate (SFR) was estimated by Kennicutt (1983) to be 9.5 M$_\odot$ yr^{-1} based on the high Hα luminosity, and values between 5 and 15 M$_\odot$ yr^{-1} can be found in the literature from different measurements (mostly Hα and infrared observations; e.g. Kennicutt, Tamblyn & Congdon 1994; Sanders et al. 2003; James et al. 2004).

The asymmetric shape of NGC 2276, with a 'bow-shock-like' structure along its western edge and a 'tail' of gas extending towards east, and the unusually intense star formation, especially along the western edge, (the source falls in the upper range of the distribution of star-forming galaxies; see e.g. Noeske et al. 2007 for the

★ E-mail: anna.wolter@brera.inaf.it
[1] Apart from NGC 2300 and NGC 2276, the other members are NGC 2268 and IC 455 (Huchra & Geller 1982). UCG 03670, at 16 arcmin ($\sim$0.15 Mpc) from NGC 2300, is likely another group member.
[2] From the NASA/IPAC Extragalactic Database (NED) http://ned.ipac.caltech.edu/ and adopting $H_0 = 73$ km s^{-1} Mpc^{-1}

scatter-plots of galaxies in the Aegis field) have attracted considerable attention but, while it is quite clear that these features are due to interaction with the environment, no consensus on the dominant physical process involved has yet been reached.

Since NGC 2300 and NGC 2276 are relatively close to each other (7 arcmin, about 70 kpc), a prime candidate is the tidal interaction between the two galaxies (Elmegreen et al. 1991; Gruendl et al. 1993; Davis et al. 1996, 1997). Other processes involved in shaping NGC 2276 are the viscous and the ram-pressure stripping of the galactic gas in the IGM (Nulsen 1982; Rasmussen, Ponman & Mulchaey 2006). Rasmussen et al. (2006) questioned the importance of the tidal interactions and argued that turbulent viscous and ram-pressure stripping, ram pressure compression of the disc gas and starburst outflows are more likely the main elements influencing the shape and SFR of NGC 2276.

Using an *XMM–Newton* observation carried out in 2001, Davis & Mushotzky (2004) identified a bright X-ray source (XMMU J072649.2+854555) at the western edge of the galaxy with an ultraluminous X-ray source (ULX: non-nuclear sources with X-ray luminosities in excess of $L_X = 10^{39}\,\mathrm{erg\,s^{-1}}$; see e.g. Feng & Soria 2011 for a review) candidate. The X-ray luminosity of this object in the 0.5–10 keV band was $L_X^{0.5-10\,\mathrm{keV}} = 1.1 \times 10^{41} d_{45.7}^2 = 5.7 \times 10^{40} d_{32.9}^2\,\mathrm{erg\,s^{-1}}$ (where d_N stands for the distance in units of N Mpc), making it one of the most luminous known in its class (e.g. Sutton et al. 2012). They also observed that the nuclear source, undetected in the *XMM–Newton* data, was much dimmer (by a factor of ∼10 at least) than the *ROSAT*/HRI nuclear source seen by Davis et al. (1997) 8 yr earlier at $L_X^{0.5-2\,\mathrm{keV}} \sim 2 \times 10^{40} d_{45.7}^2 = 10^{40} d_{32.9}^2\,\mathrm{erg\,s^{-1}}$.

ULXs are mainly found in galaxies with high SFRs, and indeed most might be assumed to be the extension of the high-mass X-ray binaries (HMXB) population to high X-ray luminosities. For instance, in The Antennae (Zezas & Fabbiano 2002), in the Cartwheel galaxy (Wolter & Trinchieri 2004), in the NGC 2207/IC 2163 pair and in NGC 4088 the X-ray luminosity function (XLF) follows the 'universal' law found by Grimm, Gilfanov & Sunyaev (2003) for HMXBs when scaled for the SFR. This assumption, linked to the proposed influence of low metallicity on the evolution of massive stars (see Mapelli et al. 2010, and references therein) leads to expect not one, but a large number of ULXs in NGC 2276. Using the correlations by Mapelli et al. (2010) and assuming a metallicity $Z = 0.22\,\mathrm{Z_\odot}$ and an SFR of $10\,\mathrm{M_\odot\,yr^{-1}}$, we expect about 10 ULXs. The metallicity is derived applying the Pilyugin & Thuan (2005) calibration on the dereddened [O II λ 3727]/Hβ and [O III λ5007]/Hβ ratios measured by Kennicutt (1992) on an integrated spectrum of NGC 2276. Indeed, a high-spatial-resolution observation of NGC 2276 taken with *Chandra* (Obs.ID 4968, PI: Rasmussen) revealed that the bright ULX candidate is actually composed of a few different sources (Wolter et al. 2011), and showed a total of 8–9 sources bright enough ($L_X > 10^{39}\,\mathrm{erg\,s^{-1}}$) during the observation to be classified as ULXs (Liu 2011; Wolter et al. 2011).

The *Chandra* data allowed Rasmussen et al. (2006) to resolve details of the X-ray morphology of NGC 2276, which, as seen at other wavelengths, is characterized by a shock-like feature along the western edge and a low surface brightness tail extending to the east. Spatially resolved spectroscopy shows that the data are consistent with the disc gas being pressurized at the leading western edge of NGC 2276, due to the galaxy moving supersonically through the IGM, at a velocity of ≈900 km s^{-1}. Rasmussen et al. (2006) estimated that the diffuse hot gas in the disc of NGC 2276 has a temperature of $kT \sim 0.3$ keV and an X-ray luminosity of $L_X^{(0.3-2.0\,\mathrm{keV})} = 1.9 \times 10^{40} d_{36.8}^2 = 1.5 \times 10^{40} d_{32.9}^2\,\mathrm{erg\,s^{-1}}$, with an inferred residual component of unresolved X-ray binaries of about 10–15 per cent of the total flux. The IGM, as observed by *Chandra*, has a profile consistent with the previous *ROSAT* measurements (Davis et al. 1996), a temperature of $kT \approx 0.9$ keV and $Z = 0.17\,\mathrm{Z_\odot}$ (Rasmussen et al. 2006). This metallicity is well matched, given also the different method used, to the one used above.

In Wolter et al. (2011), we reported on the several new ULXs observed by *Chandra* in NGC 2276 and on the fact that the bright ULX candidate XMMU J072649.2+854555 actually consists of a number of distinct sources (see also Sutton et al. 2012). In this work, we give more details on the point sources, presenting the whole *Chandra* data analysis, investigate the main mechanisms at work in shaping the galaxy by means of numerical simulations, and discuss their influence on the X-ray source population.

2 ANALYSIS OF *CHANDRA* DATA

The *Chandra* observation (Obs. ID 4968, see Rasmussen et al. 2006 for further details) was performed on 2004 June 23 with the Advanced CCD Imaging Spectrometer (ACIS; Garmire et al. 2003), and lasted about 45.8 ks. The ACIS was operated in the standard timed exposure full-frame mode, with the 'very faint' telemetry format, and NGC 2276 was positioned on the back-illuminated chip S3 (CCD7). The data were reprocessed with the *Chandra* Interactive Analysis of Observations software package (CIAO, version 4.6).[3] We removed the pixel randomization, since it deteriorates the spatial resolution, but, other than that, we followed standard data reduction and analysis procedures.

The first step of our analysis was to run the CIAO wavelet source-detection algorithm with SIGTHRESH[4] set to 10^{-6}, so that we expect at most one spurious source in the area under examination given that we consider only a single CCD. The routine found 41 sources in CCD7, of which 16 in the galaxy area, defined by $D25 = 177.1$ arcsec (de Vaucouleurs et al. 1991) with a signal-to-noise ratio higher than 4.

Source positions (in RA order) and statistics of the 16 sources are given in Table 1, while in Fig. 1 they are shown in the X-ray image and overplotted on an optical image of the galaxy. Source counts were extracted from circular regions centred at the positions found by the source-detection routine and with radius 2 arcsec. The sources are all at <2 arcmin from the aimpoint, therefore the 2 arcsec circle is large enough to include more than 90 per cent of all counts[5] and is a very good match to the ellipse from the detection algorithm. We expect a very small contribution in the area from both the instrumental and the diffuse background. The dominant source of error is statistic. For source S7, which corresponds to the nuclear region, we extracted counts in a circle of 50 arcsec radius (excluding all the detected sources in that area) for consistency with the Rasmussen et al. (2006) analysis (see Section 4). The sources' positions are plotted in Fig. 1 and the extraction area for S7 is indicated as the green circle. Instrumental and cosmic background was estimated from circular regions outside of the galaxy, but as close as possible to it, and excluding detected sources. We did not attempt to subtract the diffuse gas contribution, which is, at any rate, negligible in the extraction area of the point sources (less than 1 count per source). A first indication of the sources' spectral shape

[3] http://cxc.harvard.edu/ciao/

[4] See http://cxc.harvard.edu/ciao/ahelp/wavdetect.html for the parameters of WAVDETECT.

[5] See e.g. fig. 4.7 in http://cxc.harvard.edu/proposer/POG/html/chap4.html

Table 1. Source detected in NGC 2276. Positions from the detection algorithm and net counts from the extraction regions of 2 arcsec radius (see the text). No astrometric correction has been applied and therefore the positional uncertainty is the standard *Chandra* one of $\Delta \leq 0.6$ arcsec (90 per cent c.l.).

Number	RA (J2000)	Dec. (J2000)	Net counts (0.3–5 keV)
S1	$07^{h}26^{m}37^{s}.4$	$+85^{\circ}45'34''.5$	417.4 ± 20.4
S2	$07^{h}26^{m}43^{s}.5$	$+85^{\circ}45'00''.1$	46.2 ± 6.9
S3	$07^{h}26^{m}46^{s}.1$	$+85^{\circ}45'38''.5$	43.2 ± 6.6
S4	$07^{h}26^{m}47^{s}.9$	$+85^{\circ}45'52''.3$	175.8 ± 13.3
S5	$07^{h}26^{m}48^{s}.1$	$+85^{\circ}45'54''.9$	338.6 ± 18.4
S6	$07^{h}26^{m}48^{s}.2$	$+85^{\circ}45'49''.0$	104.7 ± 10.2
S7[a]	$07^{h}27^{m}13^{s}.0$	$+85^{\circ}45'16''.0$	40.3 ± 6.4
S8	$07^{h}27^{m}14^{s}.9$	$+85^{\circ}46'11''.5$	14.2 ± 3.9
S9	$07^{h}27^{m}15^{s}.4$	$+85^{\circ}45'54''.9$	8.2 ± 3.0
S10	$07^{h}27^{m}19^{s}.7$	$+85^{\circ}46'32''.9$	19.2 ± 4.5
S11	$07^{h}27^{m}25^{s}.8$	$+85^{\circ}45'25''.9$	68.2 ± 8.3
S12	$07^{h}27^{m}28^{s}.7$	$+85^{\circ}45'11''.1$	21.3 ± 4.7
S13	$07^{h}27^{m}53^{s}.3$	$+85^{\circ}46'08''.8$	53.2 ± 7.3
S14	$07^{h}27^{m}58^{s}.4$	$+85^{\circ}44'37''.9$	19.3 ± 4.5
S15	$07^{h}28^{m}16^{s}.0$	$+85^{\circ}44'36''.4$	29.2 ± 5.5
S16	$07^{h}28^{m}19^{s}.7$	$+85^{\circ}44'28''.5$	13.3 ± 3.7

Notes. [a]Source S7 is the centre of the galaxy: for subsequent analysis counts have been extracted in a circle of 50 arcsec radius, excluding all detected sources, resulting in a total of 1413 ± 67 net counts.

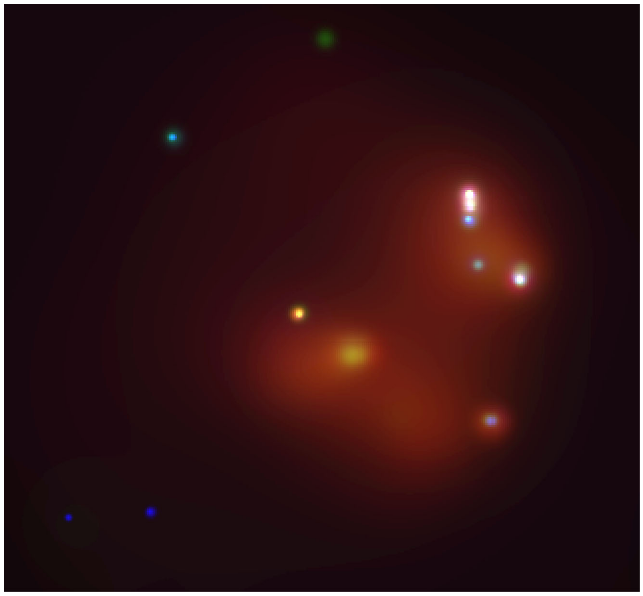

Figure 2. Three colour image of the *Chandra* data. Smoothed with CSMOOTH from CIAO in the 0.3–0.9, 0.9–1.5 and 1.5–8 keV bands for red, blue and green, respectively. Many point sources appear blue/green indicating excess absorption and/or hard spectra.

can be evinced from Fig. 2 in which the 'true' colour image of the X-ray emission has been constructed. The absorbed or flat sources appear as blue/green in this image. For a more formal analysis, we extracted individual spectra for the sources with more than a hundred net counts (S1, S4, S5, and S6, plus the extended region around S7). For the other sources (S2, S3, S8, S9, S10, S11, S12, S13, S14, S15, S16), since the paucity of counts hinders individual fits, we extracted a cumulative spectrum, which contains 336 ± 20 net counts. All the spectral analysis was performed with the XSPEC

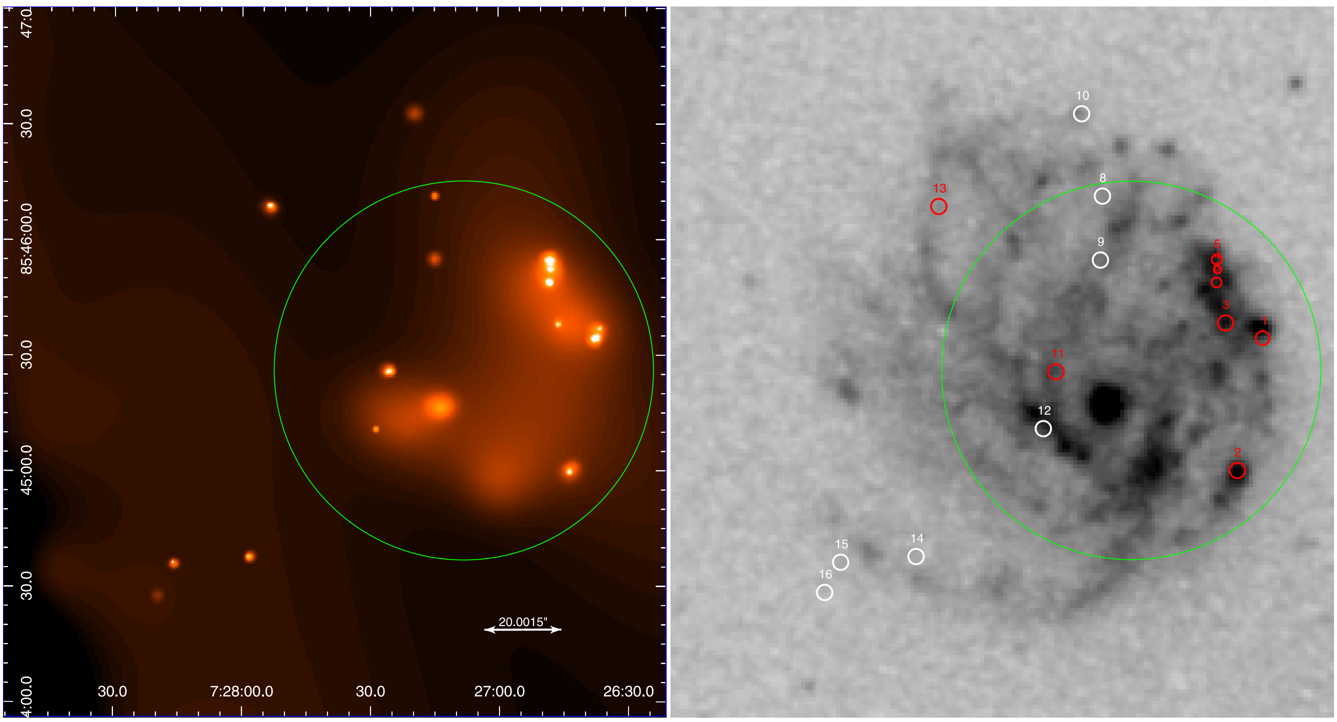

Figure 1. Left: smoothed image (CSMOOTH) from *Chandra* data in the 0.5–7 keV band. The green circle (radius=50 arcsec) indicates the region used to extract the diffuse component spectrum (associated to S7, see the text for details). Right: the X-ray sources' positions are overplotted on the optical image of NGC 2276 taken from the Digitized Sky Survey (DSS), see http://archive.stsci.edu/dss/index.html. Open circles and numbers identify detected point sources; red sources are ULXs. White sources have $L_X^{0.5-10} \leq 10^{39}$ erg s^{-1}.

(v. 12.8.0) fitting package (Arnaud 1996). Results and analysis of the spectra are described in the next sections.

3 POINT SOURCES AND ULXS

The distribution of the detected sources follows roughly the position of the arms of NGC 2276 and the zones of high activity in the other bands. Contamination from background sources may be estimated according to the $\log N - \log S$ distribution of Hasinger et al. (1993). At the detection limit of $F_X^{(0.5-2\,\mathrm{keV})} = 7 \times 10^{-16}$ erg cm^{-2} s^{-1} (which corresponds to $L_X \approx 10^{38}$ erg s^{-1} at the distance of NGC 2276), we expect 1.4 sources by chance in the total area covered by the galaxy. Therefore, at least one of the fainter sources is probably a background source.

The few bright sources with enough counts (∼100–400) to allow individual spectral fits are modelled by a simple power law modified for the interstellar absorption. A satisfactory description of their spectra has a hydrogen column density N_H of a few 10^{21} cm^{-2} (the total Galactic N_H in the direction of NGC 2276 is $\sim 5.7 \times 10^{20}$ cm^{-2}; Kalberla et al. 2005) and slopes between $\Gamma = 1.4$ and 2.2. The observed normalized net count distribution with the best-fitting model is plotted in Fig. 3, while the fit results are listed in Table 2. These spectra are consistent with typical results for ULXs when only low-count-statistics spectra are available (e.g. Swartz et al. 2004). For the other sources, we considered the cumulative spectrum (see Section 2) for a total of ∼300 net counts. An absorbed power law can be fit also to these data, resulting in an absorbing column $N_H = (1.7 \pm 0.9) \times 10^{21}$ cm^{-2} and photon index $\Gamma = 1.9 \pm 0.4$ (see Fig. 4). This mean spectrum was used to convert the observed count rates of the faintest sources into fluxes, see Table 3.

The number of sources with $L_X^{(0.5-10\,\mathrm{keV})} \geq 10^{39}$ erg s^{-1} is eight. Liu (2011) classify nine sources as ULXs, however the two lists have only the five brightest objects in common (S1, S4, S5, S6, S11). The faintest ones are not in the Liu (2011) list since they use a cutoff luminosity of $2. \times 10^{39}$ erg s^{-1} in the 0.3–8 keV band and a different distance of $D = 36.8$ Mpc. The other sources in the Liu (2011) list which are not listed here are: NGC2276-X4, which is the F8 star SAO 1148 (e.g. from the Simbad Astronomical Database[6]); NGC2276-X6 which is outside the optical region of the galaxy ($D25 = 177.1$ arcsec from NED) at ∼2 arcmin from the nucleus of the galaxy; NGC2276-X7 which is on the border of the CCD and did not survive our thresholds; NGC2276-X9 which is on the next chip S2 (CCD6) which we did not even analyse. A comparison of *XMM–Newton* and *Chandra* images of the field of the *XMM–Newton* ULX candidate XMMU J072649.2+854555 is shown in Fig. 5. Instead of a single bright source, *Chandra* found five distinct sources (S1, S3, S4, S5, and S6; all in the ULX luminosity range, plus a possible other source near S1, which is visible also in Fig. 1 but the detection algorithm is unable to pick it up) roughly following the *XMM–Newton* isophotes (see also Wolter et al. 2011). The luminosity of these sources ranges from a few 10^{39} to a few 10^{40} erg s^{-1} (Tables 2 and 3).

To investigate possible variability of the *Chandra* sources in the region of XMMU J072649.2+854555, we can compare the total luminosity from Davis & Mushotzky (2004) ($L_X^{0.5-10\,\mathrm{keV}} = 1.1 \times 10^{41} d_{45.7}^2$ erg s^{-1}$= 5.7 \times 10^{40} d_{32.9}^2$ erg s^{-1}) to that of the region in the *Chandra* data set corresponding to the *XMM–Newton* point spread function (PSF), which we chose as a circle of 30 arcsec radius centred at the *XMM–Newton* position. This includes

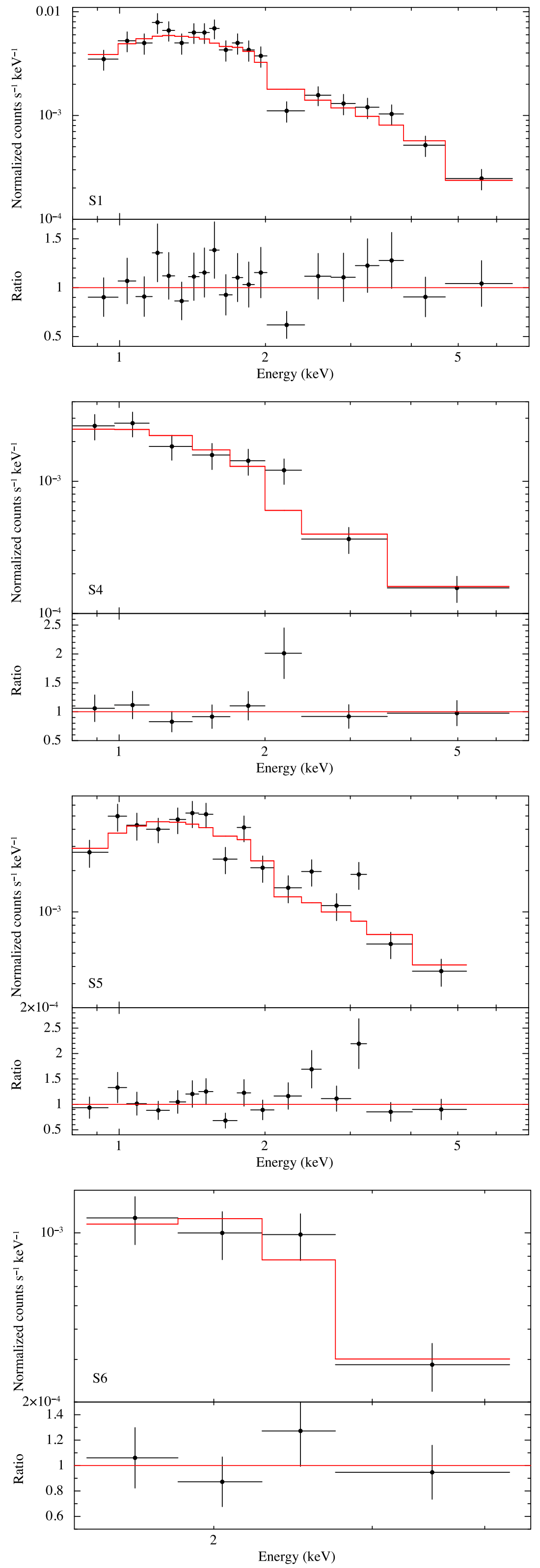

Figure 3. Spectroscopy of the four brightest ULXs (S1, S4, S5, S6). For each source (as indicated in each plot), we show the spectrum, the best-fitting power-law model (solid line) and, in the bottom panel, the ratio to the model.

[6] http://simbad.u-strasbg.fr/simbad/

Table 2. Results of spectral fit for the four ULXs with more than 100 net counts and for the sum of the fainter sources. Unabsorbed fluxes and luminosities are in the 0.5–10 keV energy band.

Name	Γ	N_H (10^{21} cm^{-2})	$F_X^{(0.5-10\,keV)}$ (10^{-14} erg cm^{-2} s^{-1})	$L_X^{(0.5-10\,keV)}$ (10^{39} erg s^{-1})	$L_X^{(2-10\,keV)}$ (10^{39} erg s^{-1})	χ^2_ν (dof)
S1	1.96 ± 0.34	4.1 ± 2.0	14.45 ± 0.71	18.7	10.29	0.92 (17)
S4	$1.48^{+0.49}_{-0.25}$	<25.0	6.78 ± 0.51	8.73	6.39	1.47 (5)
S5	1.77 ± 0.40	3.1 ± 2.0	11.10 ± 0.60	14.3	8.90	1.54 (13)
S6[a]	>3.2	6.0 ± 4.0	2.60 ± 0.25	3.36	2.86	1.50 (1)
SUM	1.93 ± 0.35	1.7 ± 0.9	6.00 ± 0.37	7.74	4.41	1.11 (18)

Note. [a]Flux and luminosities were computed with $\Gamma = 3.2$ and the fitted value for $N_H = 25.3 \times 10^{21}$ cm^{-2}.

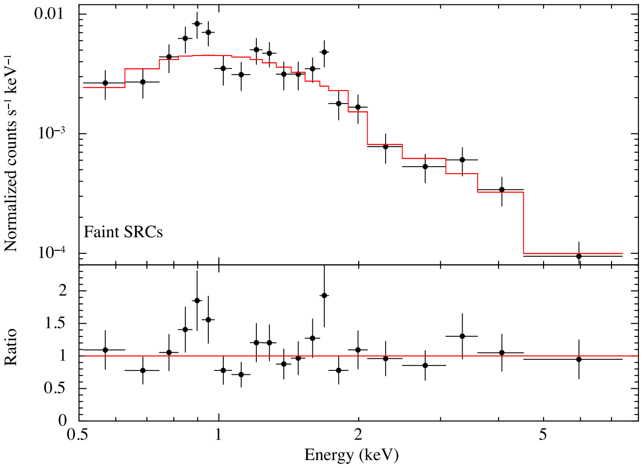

Figure 4. Combined spectrum of the fainter sources (see Section 2). The solid line indicates the best- fitting power-law model and in the bottom panel we plotted the ratio to the model.

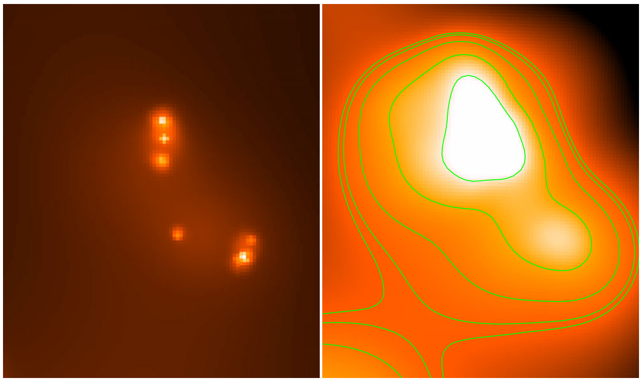

Figure 5. Field of the ULX candidate XMMU J072649.2+854555 as imaged by *Chandra* (left) and *XMM–Newton* (right) in the 0.3–8 keV energy band. Each image side is 55 × 46 arcsec wide. The green contour levels are logarithmically spaced from 0.1 cts sq.pix^{-}1. Several distinct X-ray sources are resolved by *Chandra*.

Table 3. Point source unabsorbed fluxes and luminosities computed from the power-law fit to the mean spectrum of the fainter sources (see Sections 2 and 3).

Name	$F_X^{(0.5-10\,keV)}$ (10^{-14} erg cm^{-2} s^{-1})	$L_X^{(0.5-10\,keV)}$ (10^{39} erg s^{-1})	$L_X^{(2-10\,keV)}$ (10^{39} erg s^{-1})
S2	0.96 ± 0.14	1.24	0.70
S3	0.90 ± 0.14	1.16	0.66
S8	0.30 ± 0.08	0.38	0.22
S9	0.17 ± 0.06	0.22	0.13
S10	0.40 ± 0.09	0.52	0.29
S11	1.42 ± 0.17	1.83	1.04
S12	0.44 ± 0.10	0.57	0.32
S13	1.11 ± 0.15	1.43	0.81
S14	0.40 ± 0.09	0.52	0.29
S15	0.61 ± 0.11	0.79	0.44
S16	0.28 ± 0.08	0.36	0.20

sources S1, S3, S4, S5 and S6, plus the unresolved sources and diffuse component. We extract a spectrum and fit it with the Davis & Mushotzky (2004) best-fitting model (DISKBB+MEKAL, see their table 1), leaving the normalization free. We obtain an unabsorbed luminosity $L_X^{0.5-10\,keV} = 5.1 \times 10^{40} d^2_{32.9}$ erg s^{-1}, which is consistent within uncertainties with the expectation. We make the same comparison also for the other two sources detected in both the *Chandra* and the *XMM–Newton* observation, namely source XMMU J072718.8+854636 (which corresponds to source S10), and source XMMU J072816.7+854436 (which corresponds to S15). If we consider the model of Davis & Mushotzky (2004) for each of the two sources, we find that XMMU J072718.8+85463 is apparently fainter by 1 dex ($L_X^{0.5-10\,keV} = 5.2 \times 10^{38}$erg s^{-1}) with respect to the expectation of $L_X^{0.5-10\,keV} = 4.2 \times 10^{39} d^2_{45.7}$ erg s^{-1}= $2.2 \times 10^{39} d^2_{32.9}$ erg s^{-1}). However, if we consider a region of 30 arcsec around S10, we detect in *Chandra* 158 ± 46 counts, from the diffuse contribution of the galaxy besides the 19.2 net counts from S10: therefore, it is probable that the *XMM–Newton* detection was similarly contaminated by the plasma component. A different situation is found for XMMU J072816.7+854436 which is quite isolated: the *Chandra* luminosity for a power-law spectrum is about a factor of 1.4 higher ($L_X^{0.5-10\,keV} = 7.9 \times 10^{38}$erg s^{-1}) than expected from *XMM–Newton* : $L_X^{0.5-10\,keV} = 1.1 \times 10^{39} d^2_{45.7}$ erg s^{-1}= $5.7 \times 10^{38} d^2_{32.9}$ erg s^{-1}, which however we deem not compelling given the uncertainties in spectral shape and the different response matrices of the two instruments. In conclusion, the possible small variation in flux between the observations, given the different spatial resolution of the instruments, cannot be confirmed statistically.

We note that source S6 is possibly coincident with a triple radio source of total $L_{5\,GHz} = 9.51 \times 10^{36}$ erg s^{-1}, which Mezcua et al. (2013) suggest could be the first evidence of an extended jet in a non-nuclear source. The presence of jets in ULXs has been invoked in a few cases (see also Cseh et al. 2014) but the evidence is not firm yet. The source has a very blue (hard) colour in Fig. 2 which might indicate an excess absorption. This however is not enough to imply that the source is a background source since high levels of absorption are known to be intrinsic to many ULXs.

3.1 The XLF

In order to construct the XLF of NGC 2276, we have to assess two possible sources of contamination: spurious, unwanted sources which add to the XLF, and missing sources due to detection uncertainties. We also do not include the central source (S7). To account for the possible presence of spurious contamination from background sources among the *Chandra* point sources, we randomly excluded one of the three faintest sources, following the results of Section 3 for a chance coincidence of 1.4 source at the faintest fluxes. The contamination becomes less than 0.2 sources in the entire galaxy, as defined by the *D*25 diameter, at fluxes $F_X \geq 10^{-14}$ erg cm^{-2} s^{-1}. To correct for incompleteness, we base our assessment on fig. 12 from Kim & Fabbiano (2003) in which the detection probabilities as a function of background counts and source counts are plotted. The background includes both diffuse emission from the galaxy and field background and is estimated in the case of NGC 2276 to be at a level of 0.15 counts pixel^{-1} (by averaging total counts in the galaxy region, up to *D*25, after excluding detected sources). We use the second panel, relative to a 2 arcmin off-axis, since the whole galaxy is within this limit. We apply the interpolated correction to all sources with less than 22 counts. This is a conservative estimate. In Fig. 6, we compare the resulting XLF with that of the Cartwheel galaxy, one of the richest galaxies in ULXs (Wolter & Trinchieri 2004). The Cartwheel XLF was corrected with the same procedure: in this case the background is lower (0.05 counts pixel^{-1}) and therefore we corrected only sources with less than 10 counts. Just to give an indication, the slope of the resulting XLF is $\alpha_N = -0.71 \pm 0.03$ for NGC 2276 and $\alpha_C = -0.75 \pm 0.05$ for the Cartwheel. These numbers become lower ($\alpha_N = -0.66$ and $\alpha_C = -0.60$) if we restrict the fit to the $\log L_X \leq 39.8$, consistent with the 'universal' luminosity function slope of $\alpha = -0.60$ found by e.g. Grimm, Gilfanov & Sunyaev 2003; Swartz et al. 2011; Mineo, Gilfanov & Sunyaev 2012a for HMXB and proposed to scale with the SFR. The XLF from Grimm et al. (2003) is also plotted in Fig. 6 for two different values of the SFR of 5 and 15 M$_\odot$ yr^{-1}. Also, by comparing the total X-ray luminosity or the number of ULXs with the formulas of Grimm et al. (2003), similar results are obtained: SFR = 5 and 5.5 M$_\odot$ yr^{-1}, respectively. These values are in the same range of SFR derived in other wavebands (see Section 1). Also equation 20 from Mineo et al. (2012a) gives a predicted number of sources with $L_X > 10^{38}$ erg s^{-1}=3.2 × SFR ≥ 16, consistent with the number of sources found, taking into account that at least one is spurious and the incompleteness of detection at the limit.

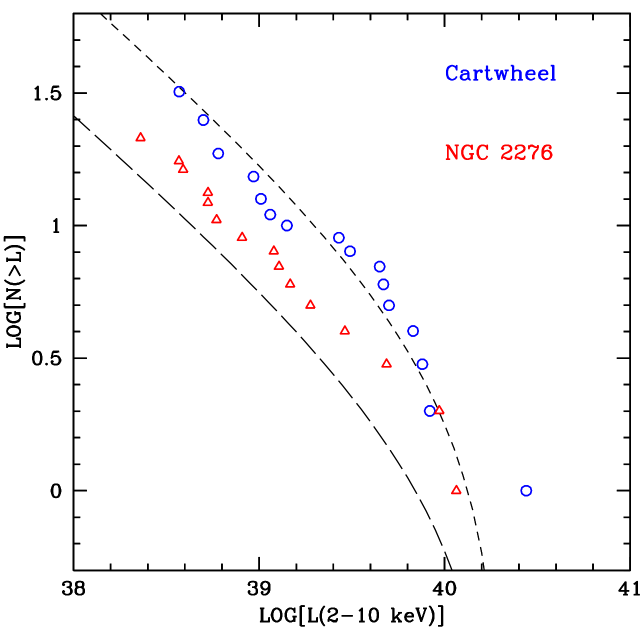

Figure 6. The XLF of NGC 2276 computed in the 2–10 keV band by using the sources detected in the galaxy area by *Chandra*. The nucleus has been removed, as well as one of the faint sources, to account for the expected contamination from background sources (see Section 3). The solid lines represent the universal XLF for HMXB by Grimm et al. (2003), normalized to 5 (long-dashed line) and 15 M$_\odot$ yr^{-1} (short-dashed line).

4 THE DIFFUSE EMISSION COMPONENT

The nuclear source of NGC 2276 was previously detected with *ROSAT* as variable (Davis et al. 1997) at $L_X^{(0.5-2\,\mathrm{keV})} \sim 2 \times 10^{40} d_{45.7}^2 = 10^{40} d_{32.9}^2$ erg s^{-1}. Notably, the source was not detected in the 2004 *XMM–Newton* observation, which set an upper limit of $L_X^{(0.5-10\,\mathrm{keV})} < 1.2 \times 10^{39} d_{32.9}^2$ erg s^{-1} on its emission. However, a correct comparison of the flux would need a detailed modelling of the surrounding emission, given the different resolution of the instruments that have observed NGC 2276 through the years. Source S7, coincident with the optical nucleus of the galaxy, is extended as we show in Fig. 7, where we compare it with the *Chandra* PSF derived with CHART with standard procedures at the position of the nucleus. We plot two different profiles in the NE and SW directions (110°–200° and 280°–370°, respectively) to show the different extent at large radii in the two directions, as already noted by Rasmussen et al. (2006).

Since the diffuse emission of NGC 2276 and in its proximity was studied in detail by Rasmussen et al. (2006), we just verify the consistence of our results for the diffuse emission of the disc (after removing the point sources) for their region A (see their fig. 2). We used an extraction region as similar as possible to that of Rasmussen et al. (2006): a circle of 50 arcsec radius, visible in Fig. 1.

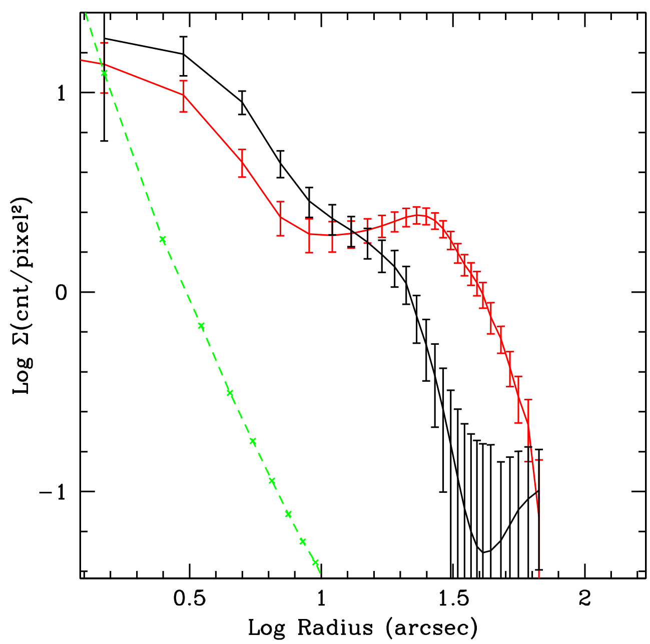

Figure 7. Profile in the direction 280°–370°, in red versus the opposite one: 110°–200°, in black. The green dashed line indicates the extent of the PSF computed via CHART, normalized to the first data point.

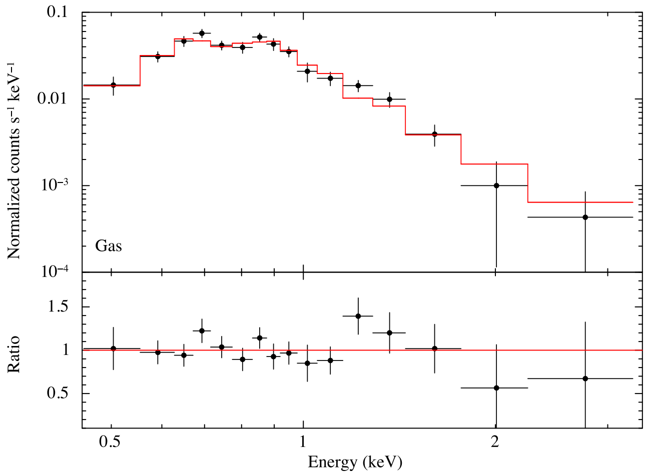

Figure 8. Spectrum of the central region of the galaxy (see Section 4). The solid line indicates the best-fitting power-law model and in the bottom panel we plotted the ratio to the model.

We make a more general hypothesis that there might be intrinsic absorption in the galaxy, and we bin the spectrum so as to have a minimum of 100 counts per bin, but we checked that the values are not very dependent on binning. In this way, in addition to the Galactic absorption, we measured an absorbing column equivalent to $N_{\rm H} = (4.2^{+1.7}_{-1.3}) \times 10^{21}$ cm^{-2} for the best-fitting [$\chi^2_\nu = 1.01$ for 13 degrees of freedom (dof)]. The resulting spectrum is plotted in Fig. 8. This results in a lower temperature of $kT = 0.18^{+0.05}_{-0.02}$ keV and an only poorly constrained photon index $\Gamma = 4 \pm 2$, but we note that the power-law component is necessary to properly fit the spectrum and we freeze it to $\Gamma = 1.7$, appropriate to represent both a low-luminosity active galactic nucleus (AGN) component and/or the unresolved point source component. The corresponding total luminosity is $L_{\rm X}^{(0.5-2\,{\rm keV})} = 1.8 \times 10^{41}$ erg s^{-1}. The luminosity of the power-law component is $L_{\rm X}^{(0.5-2\,{\rm keV})} = 2.1 \times 10^{40}$ erg s^{-1}, about 12 per cent of the total luminosity and consistent with the expectation for the unresolved point source component derived from the *K*-band luminosity of NGC 2276 $L_K = 10.7$, which corresponds to $L_{\rm X}^{2-10\,{\rm keV}} \sim 10^{40}$ erg s^{-1}, by using the relation in Kim & Fabbiano (2004). Since there should also be a fraction of unresolved HMXBs, this leaves little room for a powerful AGN.

We observe that our revised temperature and luminosity have essentially no impact on the results of Rasmussen et al. (2006), actually, the higher luminosity and lower temperature enforce their conclusion that diffuse X-ray emission from the western edge does not arise from a shock-compressed gas component.

If we compute the total emission from the *D*25 of the galaxy, then the diffuse component is $L_{\rm X}^{0.5-2\,{\rm keV}} \sim 2.5 \times 10^{41}$ erg s^{-1}: we can compare it with the findings of Mineo, Gilfanov & Sunyaev (2012b) that $L_{\rm X}^{\rm diffuse}/{\rm SFR} = 1.5 \times 10^{40}$ erg s^{-1} / (M$_\odot$ yr^{-1}), albeit with a large scatter of $\sim$ a dex and very model dependent. Again this gives an SFR in the range 5–25 M$_\odot$ yr^{-1}.

We recall also that the source is immersed in an IGM component: we report the parameters found by Davis et al. (1996) using *ROSAT* data, rescaled to our distance, which we will exploit for the subsequent simulations. They found an extent of about 25 arcmin (0.24 Mpc) for the X-ray emitting IGM, centred close to, but not exactly on, the central elliptical galaxy NGC 2300. The surface brightness of the medium is described by a King function with core radius $r_0 \sim 4.3$ arcmin and index $\beta = 0.41$, and has a luminosity of $L_{\rm X}^{\rm bol} = 1.12 \times 10^{42} d_{45.7}^2 = 5.8 \times 10^{41} d_{32.9}^2$ erg s^{-1}. The mass of the hot intragroup gas is $M_{\rm gas} = (1.25 \pm 0.13) \times 10^{12}$ M$_\odot$. Rasmussen et al. (2006) find similar values, but the *ROSAT* larger field of view is better suited to measure this large extent component.

5 WHERE DOES THE MORPHOLOGY OF NGC 2276 COME FROM?

Whether the perturbed morphology of NGC 2276 is the result of tidal interactions with NGC 2300, or of ram pressure stripping is still an open question. The simplest way to estimate the importance of tidal forces, without running a simulation, is to compare the centripetal acceleration of NGC 2276 ($a_{\rm c}$) to the radial acceleration ($a_{\rm r}$) exerted by the other galaxies in the group, which is dominated by NGC 2300 and by the hot gas component:

$$a_{\rm c}(r) = \frac{G\,M(r)}{r^2}, \qquad (1)$$

$$a_{\rm r}(D) = G\,M_{\rm group}(D)\left[\frac{1}{D^2} - \frac{1}{(D+r)^2}\right], \qquad (2)$$

where r and $M(r)$ are the three-dimensional distance from the centre of NGC 2276 and the mass of NGC 2276 inside r, respectively, while $M_{\rm group}(D)$ is the mass of the group enclosed within a distance D from the centre of NGC 2300.

To derive the actual distance between NGC 2276 and NGC 2300, we used the velocity of NGC 2276 with respect to the IGM, derived assuming that the IGM is coupled to NGC 2300. Rasmussen et al. (2006) derive a Mach number of $\mathcal{M} = 1.70 \pm 0.23$, corresponding to a three-dimensional velocity of $v = v_{\rm s} \times \mathcal{M} = 865 \pm 120$ km s^{-1}. The distance $D = x/\cos\alpha$ is then derived by measuring $x = 83.2$ kpc (the distance between the centres of the two galaxies projected on the plane of the sky) and $\cos\alpha = \Delta v_{\rm r}/v$, where $\Delta v_{\rm r} = 421$ km s^{-1} is the relative recession velocity between the two galaxies (Rasmussen et al. 2006). The three-dimensional distance between the two galaxies is then 170 kpc, under these assumptions.

For $r = 13$ kpc (which is approximately the isophotal radius of NGC 2276) and $M(13\,{\rm kpc}) = 2 \times 10^{11}$ M$_\odot$, we obtain $a_c = 1.6 \times 10^{-8}$ cm s^{-2}. For $D = 170$ kpc, $a_r(D) \sim 5 \times 10^{-10}$ cm s^{-2}. Thus, we expect tidal forces to be small today, when compared with the self-gravity of the galaxy. Let us consider now the importance of ram-pressure stripping. The distance from the centre of a galaxy at which ram-pressure stripping becomes important can be evaluated as (Yoshida et al. 2008)

$$r_{\rm rp} = \frac{h}{2}\ln\left(\frac{G\,M_*\,M_{\rm ISM}}{2\,\pi v^2 \rho_{\rm IGM}\,h^4}\right), \qquad (3)$$

where h is the scalelength of the disc, M_* and $M_{\rm ISM}$ are the total stellar mass and interstellar medium mass of the galaxy, v is the relative velocity between the galaxy and the IGM, and $\rho_{\rm IGM}$ is the local density of IGM. If we assume $h = 3$ kpc, $M_* = 2.8 \times 10^{10}$ M$_\odot$, $M_{\rm ISM} = 8 \times 10^9$ M$_\odot$, $v = 850$ km s^{-1} and $\rho_{\rm IGM} = 5 \times 10^{-27}$ g cm^{-3}, which are consistent with the observations of NGC 2276 (Davis et al. 1996; Rasmussen et al. 2006) and its environment (we use the same values for the simulations described in the next section), we obtain $r_{\rm rp} = 6.5$ kpc, which is larger than h but still inside the isophotal radius of NGC 2276 (13.2 kpc). Thus, we expect ram-pressure to be quite effective in perturbing the morphology of NGC 2276.

Even if from equations (1) and (2) we have shown that tidal forces are not as efficient as ram pressure, it is reasonable to expect that there is an interplay between tidal forces and ram pressure, leading to an enhancement of NGC 2276 stripping with respect to the case in which ram pressure was the only process at work (see e.g. the argument in Yoshida et al. 2008). In addition, viscous stripping (e.g. Nulsen 1982) might also play a role, removing matter from the ISM.

6 NUMERICAL SIMULATIONS

To study the morphology of NGC 2276 in more detail than with our order-of-magnitude calculations, we ran *N*-body/smoothed particle hydrodynamics (SPH) numerical simulations of the interaction between NGC 2276 and its environment. We used the GADGET-2 code (Springel, Yoshida & White 2001; Springel 2005).

The initial conditions are taken to the simplest possible level. In all the simulations, we put NGC 2276 on a parabolic orbit around NGC 2300 (assumed to sit at the bottom of the gravitational potential well of the group). The two galaxies start from an initial separation of 170 kpc, 85 Myr before the periapsis. At periapsis, the galaxies reach their minimum distance of 160 kpc, and after another 85 Myr they reach their present separation of 170 kpc. We ran the simulations for 1 Gyr, but the most relevant effects occur during (and within $\lesssim 200$ Myr after) the periapsis passage.

We describe the elliptical galaxy NGC 2300 as a rigid potential, to reduce the computing time. We further assume that the total contribution is due to the dominant component of dark matter, described by a Navarro, Frenk and White (NFW) profile (Navarro, Frenk & White 1997):

$$\rho(x) = \frac{\rho_0}{x\,(1+x)^2}, \tag{4}$$

where $x = \frac{r}{r_s}$, with $r_s = R_{200}/c$ and $R_{200} = (M_{tot}\,G/H_0^2)^{1/3}$ ($H_0 = 73\,\mathrm{km\,s^{-1}\,Mpc^{-1}}$ being the Hubble constant, M_{tot} being the total mass and c being the concentration parameter), and

$$\rho_0 = \frac{200\,\rho_{crit}\,c^3}{3\,(\ln(1+c) - c/(1+c))}, \tag{5}$$

where ρ_{crit} is the current critical density of the Universe. We assume $M_{tot} = 1.3 \times 10^{13}\ \mathrm{M_\odot}$ and concentration parameter $c = 10$.

The second ingredient is the IGM. We perform three different simulations for different choices of the IGM profiles. The first is a 'dry' simulation, with no IGM. This is a control simulation aiming to isolate the purely tidal effects between the galaxies.

The second and third simulations assume that the IGM is present, but with different distributions. In both cases, the distributions are centred on NGC 2300. In both simulations, the gas is assumed to be adiabatic, with initial temperature 2×10^6 K, the total mass of gas is $M_g = 1.25 \times 10^{12}\ \mathrm{M_\odot}$ and the mass of a single gas particle is $10^6\ \mathrm{M_\odot}$ (for a total number of 1.25×10^6 particles).

In the second simulation, the IGM has an NFW profile[7] with concentration $c = 10$.

Finally, in the third simulation the gas is distributed as a King model (King 1962):

$$\rho(r) = \rho_0 \left[1 + \left(\frac{r}{r_c}\right)^2\right]^{-3\beta+0.5}, \tag{6}$$

[7] The NFW profile usually refers to dark matter, and not to baryonic matter. The rationale of adopting an NFW profile for the baryonic IGM is the following. For large radii, the NFW has the asymptotic form $\varrho \propto r^{-3}$ to be compared with the $\varrho \propto r^{-2}$ of an isothermal sphere. The NFW would model an IGM distribution concentrated close to NGC 2300, while the isothermal sphere models a more widespread IGM.

where $\rho_0 = 3.1 \times 10^{-3}\ \mathrm{cm^{-3}}$ (from Davis et al. 1996), $\beta = 0.41$ (from Rasmussen et al. 2006) and $r_c = 4.0$ arcmin (from Rasmussen et al. 2006).

The third ingredient is a model of NGC 2276. We parametrize it, according to Widrow & Dubinski (2005), as the sum of three different components: bulge, disc and dark matter halo. The total number of particles in the dark matter halo, bulge and disc of the NGC 2276 model are 2×10^6, 10^5 and 6×10^5, respectively. The softening length is 100 pc.

The dark matter halo is modelled as an NFW potential with $M_{tot} = 6 \times 10^{11}\ \mathrm{M_\odot}$ and $c = 10$. The bulge is represented by a Sérsic profile, according to the Prugniel & Simien (1997) deprojection $\rho_b(r) \propto (r/r_e)^{-p} \exp{(r/r_e)^{1/n}}$, where we assume $r_e = 0.83$ pc, $p = -1$ and $n = 1.83$. The normalization of the profile is set by the total mass of the bulge $M_b = 6 \times 10^9\ \mathrm{M_\odot}$.

The gas and the stellar component are distributed as an exponential Hernquist disc (Hernquist 1993):

$$\rho_d(R, z) = \frac{M_d}{4\pi h^2 z_0} \exp{(s - R/h)}\ \mathrm{sech}^2\,(z/z_0), \tag{7}$$

where R and z are the cylindrical coordinates, $M_d = 3.6 \times 10^{10}\ \mathrm{M_\odot}$ is the total mass of the disc, $h = 3$ kpc is the scalelength of the disc and $z_0 = 0.3$ pc is the scaleheight of the disc. The disc is composed of both gas and stellar particles, with the total mass of gas and stars being $M_{d,g} = 0.8 \times 10^{10}$ and $M_{d,*} = 2.2 \times 10^{10}\ \mathrm{M_\odot}$, respectively.

The gas component of the NGC 2276 model is assumed to be adiabatic, with initial temperature of $T = 2 \times 10^4$ K (Rasmussen et al. 2006). We do not introduce a cooling function, but verify 'a posteriori' if the cooling time t_{cool} is shorter than the dynamical free fall time t_{dyn} to estimate the rate of star formation. In particular, we estimate the cooling time as

$$t_{cool} = \frac{3}{2}\,\frac{n\,k\,T}{n_e\,n_p\,\Lambda(Z, T, n)}, \tag{8}$$

where n is the total gas density, n_e is the density of electrons, n_p is the density of protons, k is the Boltzmann constant, T is the temperature, and $\Lambda(Z, T, n)$ is the cooling function, as a function of n, T and of the metallicity Z. We used the cooling function of Sutherland & Dopita (1993).

We assume that gas is able to form stars if

$$t_{cool} < t_{dyn} < t_{life}, \tag{9}$$

where t_{life} is the lifetime of a gas clump or structure, derived directly from the simulations.

Here, below we shortly summarize the results of our simulations.

6.1 Dry simulation

Our order-of-magnitude estimate shows that tidal forces should not be very important for NGC 2276. On the other hand, even in the simulation without IGM we observe the formation of (not strongly pronounced) tidal arms in both the stellar and the gaseous components. In addition, the gas disc thickens. The regions where condition 9 is satisfied are very rare in the dry simulation, and we expect that star formation is not enhanced by the interaction, even during the periapsis passage.

No gas is stripped from the galactic disc, and the tails observed by Rasmussen et al. (2006) are not reproduced.

6.2 NFW simulation

The evolution of the disc galaxy changes significantly, if the IGM is accounted for. As we expect from our order-of-magnitude estimate, ram-pressure stripping and viscous stripping are efficient, and lead to the formation of tails already during the periapsis passage (see Fig. 9). We also see that the front side of the galaxy disc is perturbed, recalling the asymmetric 'bow-shock-like' shape of NGC 2276.

The total mass in the tails is $\sim 6 \times 10^8$ $M_{\odot}$ after the first periapsis passage (it will rise to $\sim 1 \times 10^9$ $M_{\odot}$ at the end of the simulation). A part of this mass forms clumps that are visible in Fig. 9. The cooling time in the galaxy disc is $\sim 10^{4-5}$ yr, while it is 10–20 Myr in the ram-pressure stripped tails. The dynamical time $t_{\rm dyn}$ is 200 and 10 Myr in the galaxy disc and in the tails, respectively. Thus, star formation occurs in the galaxy disc and might occur also in the tails.

Finally, a small but significant fraction of the gas component of the NGC 2276 model (8.6×10^8 $M_{\odot}$, i.e. 6.6 per cent of the entire gas component) is completely stripped and lost from the galaxy during the entire simulation.

6.3 Isothermal sphere simulation

The third simulation is very similar to the second one. Even in this simulation, ram pressure produces a deformation in the front side of the galaxy disc and leads to the formation of tails and clumps. The total mass in the tails is 6×10^8 $M_{\odot}$ after the periapsis passage, and raises to 7.5×10^8 $M_{\odot}$ at the end of the simulation, with no significant difference with respect to the second simulation. In the tails, $t_{\rm cool} \sim t_{\rm dyn} \sim 10$ Myr, suggesting that star formation is possible. In the disc galaxy, $t_{\rm cool} \sim 10^{4-5}$yr $\ll t_{\rm dyn} \sim 300$ Myr, indicating that star formation should occur.

The total mass of gas that is lost from the disc galaxy by the end of the simulation is 1.5×10^8 $M_{\odot}$, i.e. ~12 per cent of the entire initial gas mass in the NGC 2276 model. This is nearly a factor of 2 larger than in the second simulation. The difference can be explained with the fact that the IGM density goes as $\rho_{\rm IGM} \propto r^{-3}$ and $\propto r^{-2}$ in the second and in the third simulation, respectively. Since the density of the IGM at large distances from the elliptical galaxy in the third simulation is higher than that in the second simulation, we expect that ram pressure stripping will last longer than in the second simulation (i.e. it is important even when the disc galaxy is far from periapsis).

6.4 Summary of simulation results and caveats

In conclusion, we found that ram-pressure stripping and viscous stripping are the dominant processes and can lead to both the formation of the tails and the deformation of the front side of the disc galaxy. Tidal forces contribute marginally, by producing tidal arms and thickening the gaseous disc. We found a factor of 2–5 lower SFR than in the observations, but we are aware that our very approximate treatment of gas underestimates both cooling and SFR.

Moreover, the version of the SPH technique adopted in GADGET-2 is known to poorly resolve dynamical instabilities and mixing (e.g. Agertz et al. 2007). The main reason is that the SPH formulation adopted in GADGET-2 inaccurately handles the case of low-density regions in contact with high-density ones. As a consequence, gas turbulence is artificially suppressed, and gas stripping due to ram pressure might be underestimated with respect to other formalisms (e.g. grid codes). In particular, we expect that the gas mass in the stripped tails is underestimated in our simulations, and the

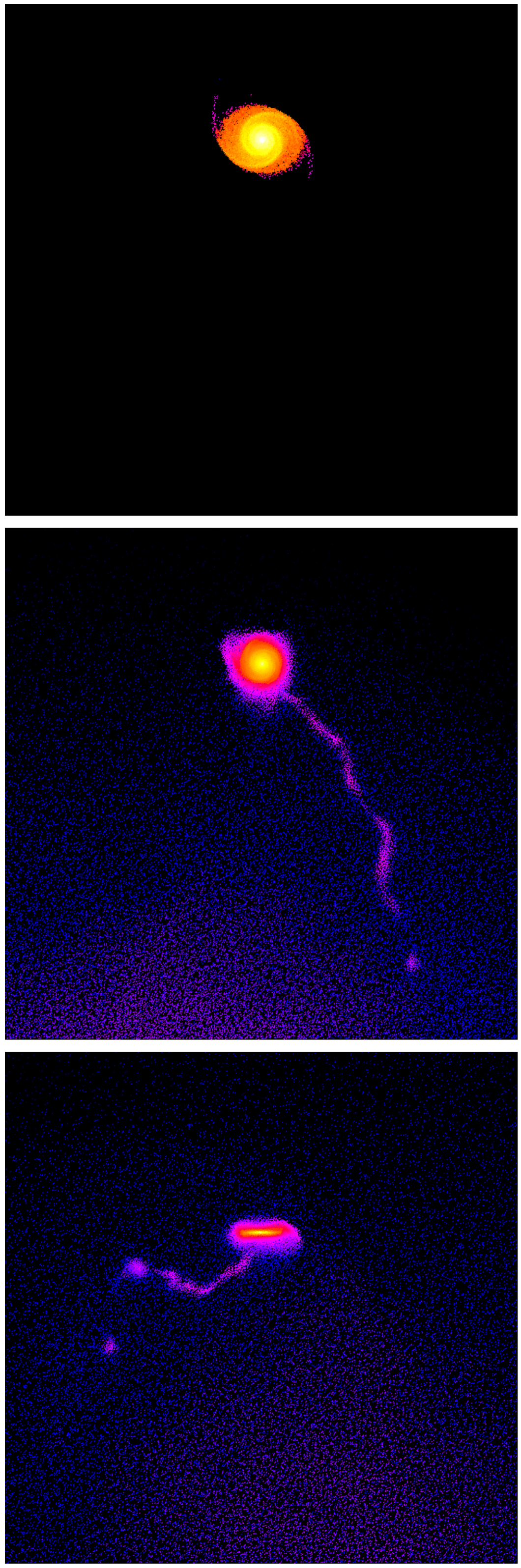

Figure 9. Colour-coded density map stars (top panel) and gas (central and bottom panel) at $t = 300$ Myr in the NFW simulation. The boxes measure 300 kpc per edge. Top panel: the density of stars has been projected along the z-axis; central (bottom) panel: the density of gas has been projected along the z-axis (y-axis). A tail structure is well visible in the *central* and *bottom* panel.

morphology of the resulting tails is quite smoother than it should be. This implies that our results can be regarded as lower limits for the ram-pressure effects. Bearing these *caveats* in mind, we conclude that our simulations are able to qualitatively reproduce the peculiar shape of NGC 2276, and to confirm the importance of ram pressure and viscous stripping.

7 SUMMARY AND CONCLUSIONS

We have analysed a *Chandra* observation of NGC 2276, a spiral galaxy in the group of the elliptical NGC 2300. We have paid particular attention to the point sources detected in the area of the galaxy. We find that a large number of ULXs are present, which makes NGC 2276 one of the richest environments for this still enigmatic bright sources.

We have seen in Wolter et al. (2011) that six of the X-ray bright sources, four of which are ULXs, are positionally coincident (1–2 arcsec) with H II regions (from Hodge & Kennicutt 1983; Davis et al. 1997). However, the spatial resolution at the distance of NGC 2276 is not enough to warrant a physical association. At least five supernovae have been observed in the last 50 yr (see Section 1 for references), two close to the centre and two in the western region where ULXs are found.

All observations concur on linking the high activity with the presence of a large number of ULXs, although there is no one-to-one correspondence between peaks in different bands, as is already seen in other galaxies, like the Cartwheel (Wolter & Trinchieri 2004). Radio emission is enhanced throughout the galaxy body: one of the sULX is possibly associated to either a radio bubble or an extended jet structure (Mezcua et al. 2013), however the complex radio field makes the interpretation difficult. The source has a very hard spectrum: we cannot exclude the possibility that it is a chance superposition with a background AGN.

We detect 15 sources associated with the galaxy NGC 2276 in the *Chandra* observation, out of which 8 are above the ULX luminosity threshold. We derive an XLF and confirm the previous estimates of the SFR of NGC 2276 in the range SFR = 5–15 $M_\odot$ yr^{-1}. The value is close to those of the Antennae and the Cartwheel, which are fitted with SFR = 7.1 $M_\odot$ yr^{-1} (Zezas & Fabbiano 2002) and ~20 $M_\odot$ yr^{-1} (Wolter & Trinchieri 2004), respectively. These numbers reconcile expectation from Mapelli et al. (2010) with observations.

We know that moderate variability is rather common in ULXs (see e.g. Crivellari, Wolter & Trinchieri 2009 and Zezas et al. 2006) and in recent years a few transient ULXs have also been identified (e.g. Sivakoff et al. 2008; Middleton et al. 2012, 2013; Soria et al. 2012; Esposito et al. 2013). We investigate, as much as possible given the different instruments used with widely different spatial resolution and response, flux variations for the bright source detected in *XMM–Newton*. We do not find any significant evidence for variability, although a better comparison could be done by using the same instrument repeatedly.

We confirm parameters for the diffuse emission as derived by Rasmussen et al. (2006), however we find that the spectrum is best fitted by adding an intrinsic absorption component that raises the unabsorbed luminosity to $L_X^{(0.5-2\,\mathrm{keV})} = 1.8 \times 10^{41}$ erg s^{-1}. The peak of this distribution is at the centre of the galaxy. The spectrum is consistent with the sum of a hot plasma diffuse component, plus an unresolved component due to active stars and binaries account for a small fraction of the total luminosity (see Section 4).

The *Chandra* data display no point source at the centre of the galaxy. A low luminosity variable AGN of $L_X \leq$ few $\times\ 10^{39}$ erg s^{-1}might lurk in the midst. However, the observational results of both the *ROSAT* HRI (Total $L_X = 3.2 \times 10^{41} d_{45.7}^2$erg s^{-1} in a 22 arcsec radius circle: Davis et al. 1997) and the *XMM–Newton* ($L_X \leq 2.4 \times 10^{39} d_{45.7}^2$erg s^{-1} above the diffuse emission: Davis & Mushotzky 2004) data sets are consistent with no point source in the centre of the galaxy. If anything, the presence of two ULX (S11 and S12) at $r \leq 30$ arcsec could be responsible for some variability on long time-scales.

We have performed a number of simulations to derive the source of activity and asymmetry in NGC 2276 and confirm that this is linked to the large number of ULXs found. Assuming a simplified scenario, we derived a morphology very reminiscent of the observed one and we derive a total mass within a factor of 2 from observations. The presence of a gas envelope around the central elliptical galaxy NGC 2300 is necessary in order to produce the effects, along the same lines as suggested by Rasmussen et al. (2006).

In conclusion, we found that ram-pressure stripping and viscous stripping are the dominant processes and can lead both to the formation of the tails and to the deformation of the front side of the disc galaxy. Tidal forces contribute marginally, by producing tidal arms and thickening the gaseous disc. Therefore, even if at a simple level, we conclude that our simulations are able to reproduce the very peculiar shape of NGC 2276 and the mass of the tidal tails.

ACKNOWLEDGEMENTS

We thank Stefano Rota and Mattia Villani for their contribution in an earlier stage of the analysis. We thank Ewan O'Sullivan for precious suggestions. We thank Dong-Woo Kim, Mar Mezcua and the referees for useful inputs that helped improve the paper. We acknowledge partial financial support from INAF through grant PRIN-2011-1 (Challenging Ultraluminous X-ray sources: chasing their black holes and formation pathways). MM and AW acknowledge financial support from the Italian Ministry of Education, University and Research (MIUR) through grant FIRB 2012 RBFR12PM1F. PE acknowledges a Fulbright Research Scholar grant administered by the US–Italy Fulbright Commission and is grateful to the Harvard–Smithsonian Center for Astrophysics for hosting him during his Fulbright exchange. (The Fulbright Scholar Program is sponsored by the US Department of State and administered by CIES, a division of IIE.) This research is based on data obtained from the *Chandra* Data Archive and has made use of software provided by the *Chandra* X-ray Center (CXC) in the application package CIAO. This research has made use of the NASA/IPAC Extragalactic Database (NED) which is operated by the Jet Propulsion Laboratory, California Institute of Technology, under contract with the NASA and of the SIMBAD data base, operated at CDS, Strasbourg, France. The Digitized Sky Surveys were produced at the Space Telescope Science Institute under US Government grant NAG W-2166. The simulations were performed with the Lagrange cluster at the Consorzio Interuniversitario Lombardo per L'Elaborazione Automatica (CILEA).

REFERENCES

Agertz O. et al., 2007, MNRAS, 380, 963
Arnaud K. A., 1996, in Jacoby G. H., Barnes J., eds, ASP Conf. Ser. Vol. 346, Astronomical Data Analysis Software and Systems V. Astron. Soc. Pac., San Francisco, p. 17
Barbon R., Cappellaro E., Turatto M., 1989, A&AS, 81, 421
Crivellari E., Wolter A., Trinchieri G., 2009, A&A, 501, 445
Cseh D. et al., 2014, MNRAS, 439, L1

Davis D. S., Mushotzky R. F., 2004, ApJ, 604, 653
Davis D. S., Mulchaey J. S., Mushotzky R. F., Burstein D., 1996, ApJ, 460, 601
Davis D. S., Keel W. C., Mulchaey J. S., Henning P. A., 1997, AJ, 114, 613
de Vaucouleurs G., de Vaucouleurs A., Corwin H. G., Jr Buta R. J., Paturel G., Fouqué P., 1991, Third Reference Catalogue of Bright Galaxies. Springer, New York
Dimai A., Migliardi M., Manzini F., 2005, IAU Circ., 8588, 2
Elmegreen D. M., Sundin M., Sundelius B., Elmegreen B., 1991, A&A, 244, 52
Esposito P., Motta S. E., Pintore F., Zampieri L., Tomasella L., 2013, MNRAS, 428, 2480
Feng H., Soria R., 2011, New Astron. Rev., 55, 166
Garmire G. P., Bautz M. W., Ford P. G., Nousek J. A., Ricker G. R., Jr 2003, in Truemper J. E., Tananbaum H. D., eds, Proc. SPIE Vol. 4851, X-Ray and Gamma-Ray Telescopes and Instruments for Astronomy. SPIE, Bellingham, p. 28
Grimm H.-J., Gilfanov M., Sunyaev R., 2003, MNRAS, 339, 793
Gruendl R. A., Vogel S. N., Davis D. S., Mulchaey J. S., 1993, ApJ, 413, L81
Hasinger G., Burg R., Giacconi R., Hartner G., Schmidt M., Trumper J., Zamorani G., 1993, A&A, 275, 1
Hernquist L., 1993, ApJS, 86, 389
Hodge P. W., Kennicutt R. C., Jr, 1983, AJ, 88, 296
Huchra J. P., Geller M. J., 1982, ApJ, 257, 423
Iskudaryan S. G., Shakhbazyan R. K., 1967, Astrophysics, 3, 67
James P. A. et al., 2004, A&A, 414, 23
Kalberla P. M. W., Burton W. B., Hartmann D., Arnal E. M., Bajaja E., Morras R., Pöppel W. G. L., 2005, A&A, 440, 775
Kennicutt R. C., Jr, 1983, ApJ, 272, 54
Kennicutt R. C., Jr, 1992, ApJ, 388, 310
Kennicutt R. C., Jr, Tamblyn P., Congdon C. E., 1994, ApJ, 435, 22
Kim D.-W., Fabbiano G., 2003, ApJ, 586, 826
Kim D.-W., Fabbiano G., 2004, ApJ, 611, 846
King I., 1962, AJ, 67, 274
Liu J., 2011, ApJS, 192, 10
Mapelli M., Ripamonti E., Zampieri L., Colpi M., Bressan A., 2010, MNRAS, 408, 234
Mezcua M., Roberts T. P., Sutton A. D., Lobanov A. P., 2013, MNRAS, 436, 3128
Middleton M. J., Sutton A. D., Roberts T. P., Jackson F. E., Done C., 2012, MNRAS, 420, 2969
Middleton M. J. et al., 2013, Nature, 493, 187
Mineo S., Gilfanov M., Sunyaev R., 2012a, MNRAS, 419, 2095
Mineo S., Gilfanov M., Sunyaev R., 2012b, MNRAS, 426, 1870
Mulchaey J. S., Davis D. S., Mushotzky R. F., Burstein D., 1993, ApJ, 404, L9
Navarro J. F., Frenk C. S., White S. D. M., 1997, ApJ, 490, 493
Noeske K. G. et al., 2007, ApJ, 660, L43
Nulsen P. E. J., 1982, MNRAS, 198, 1007
Pilyugin L. S., Thuan T. X., 2005, ApJ, 631, 231
Prugniel Ph., Simien F., 1997, A&A, 321, 11
Rasmussen J., Ponman T. J., Mulchaey J. S., 2006, MNRAS, 370, 453
Sanders D. B., Mazzarella J. M., Kim D.-C., Surace J. A., Soifer B. T., 2003, AJ, 126, 1607
Sivakoff G. R. et al., 2008, ApJ, 677, L27
Soria R., Kuntz K. D., Winkler P. F., Blair W. P., Long K. S., Plucinsky P. P., Whitmore B. C., 2012, ApJ, 750, 152
Springel V., 2005, MNRAS, 364, 1105
Springel V., Yoshida N., White S. D. M., 2001, New Astron., 6, 79
Sutherland R. S., Dopita M. A., 1993, ApJS, 88, 253
Sutton A. D., Roberts T. P., Walton D. J., Gladstone J. C., Scott A. E., 2012, MNRAS, 423, 1154
Swartz D. A., Ghosh K. K., Tennant A. F., Wu K., 2004, ApJS, 154, 519
Swartz D. A., Soria R., Tennant A. F., Yukita M., 2011, ApJ, 741, 49
Treffers R. R., Filippenko A. V., Leibundgut B., Paik Y., Lee L. F. M., Richmond M. W., 1993, IAU Circ., 5850
Widrow L. M., Dubinski J., 2005, ApJ, 631, 838
Wolter A., Trinchieri G., 2004, A&A, 426, 787
Wolter A., Pizzolato F., Rota S., Mapelli M., Ripamonti E., 2011, Astron. Nachr., 332, 358
Yoshida M., Yagi M., Komiyama Y., Furusawa H., Kashikawa N., Koyama Y., Yamanoi H., Hattori T., Okamura S., 2008, ApJ, 688, 918
Zezas A., Fabbiano G., 2002, ApJ, 577, 726
Zezas A., Fabbiano G., Baldi A., Schweizer F., King A. R., Ponman T. J., Rots A. H., 2006, ApJS, 166, 211

This paper has been typeset from a TEX/LATEX file prepared by the author.